Deciphering the role of dopants (Mn, Co, and Cu) in Ni-based CO_2 methanation catalysts

Yingrui Zhao,[a] Sandra Casale, [b] Capucine Sassoye,[c] Damien P. Debecker [a,*]

[a] Université catholique de Louvain (UCLouvain), Institute of Condensed Matter and Nanosciences (IMCN), Place Louis Pasteur, 1, box L4.01.09, 1348 Louvain-La-Neuve, Belgium.

[b] Sorbonne Université, Laboratoire de Réactivité de Surface, CNRS UMR 7197, 4 Place Jussieu, 75005, Paris, France

[c] Sorbonne Université, Chimie de la Matière Condensée de Paris, UMR 7574, 4 Place Jussieu, 75005 Paris, France.

* Corresponding autor:

E-mail: damien.debecker@uclouvain.be

ORCID: 0000-0001-6500-2996

Abstract

CO_2 methanation is effectively catalyzed by Ni-based catalysts and doping is widely applied to further enhance performance. Deciphering the role of the promoter and the mechanism of promotion is of great meaning for the development of highly active catalysts. Herein, a series of model catalysts was prepared to address this challenge. Compared to Ni/SiO_2, the Mn-doped and Co-doped catalysts showed higher methanation activity. On the contrary, the Cu-promoted catalyst showed lower performance. A comprehensive characterization study suggests that the effect of promoters is to orient the reaction mechanism and favor the conversion of key intermediates. Mn addition promotes the hydrogenation of the formaldehyde intermediate to the methoxy intermediate, which is the rate determining step of the RWGS+CO hydrogenation pathway (being dominant at low temperature, below 250 °C). Co addition facilitates the formation of formate species, which is the rate determining step of the formate pathway (proceeding in parallel with RWGS+CO hydrogenation pathway). Cu addition has a negative effect on the rate determining step of those two pathways.

Keywords

Hydrogenation of CO_2, Sabatier reaction, metal doping, Ni nanoparticles, mesoporous catalysts

1. Introduction

Anthropogenic CO_2 emissions, primarily driven by the massive combustion of fossil fuels, are a major cause of the climatic and environmental challenges we face today. CO_2 capture and storage (CCS) and CO_2 capture and utilization (CCU) have been extensively investigated and proposed as promising mitigation strategies.[1-3] In general, CO_2 can be catalytically reduced to fuels or value-added chemicals (such as carbon monoxide, methane, methanol, formic acid, ethanol, etc.).[4-9] Among these products, CH_4 is an attractive target because of its high demand and compatibility with existing natural gas infrastructure for distribution and combustion.[10] Importantly, the hydrogen used for the CO_2 methanation must be "green", i.e. derived from renewable, non-fossil resources (e.g., water electrolysis fed with renewable electricity, or photocatalysis), thereby providing a way for storing surplus intermittent renewable energy.[11, 12]

As a highly exothermic reaction, CO_2 methanation reaction ($CO_2 + 4H_2 \rightarrow CH_4 + 2H_2O$, $\Delta H_{298K} = -165$ kJ mol^{-1}) is favored at low temperatures. Furthermore, at elevated temperatures (> 200°C), CO can be formed as a byproduct, and catalyst deactivation process is accelerated.[6] On the contrary, this process is kinetically limited due to the high stability of CO_2 and the substantial energy demand to transform C^{4+} of CO_2 to C^{4-} of CH_4.[13] Therefore, the primary objective in this field is to develop highly active catalysts enable operation at relatively low temperatures while maintaining high CH_4 selectivity and long-term stability.

Supported Ni-based catalysts are the most promising candidate for the CO_2 methanation reaction due to their high CH_4 selectivity and low cost.[14] However, their low-temperature activity remains inferior to that of certain noble metal counterparts. To enhance catalytic activity, various promoters have been investigated. Literature reports are somewhat contradictory, indicating that promoters can exert multiple effects, such as altering the dispersion of the active phase (Ni nanoparticles), modifying metal reducibility during pretreatment, enhancing surface basicity, and potentially influencing reaction pathways.[15-18] For example, Wu et al. reported that Mn-doped Ni/Al_2O_3-ZrO_2 catalysts exhibited the best catalytic activity in comparison to other additives (Fe, Co, Cr).[19] In contrast, Xu et al. found that Co-doped catalysts exhibited much higher activity than the Mn-, Fe-, and Cu-doped catalysts in the Ni/$Ce_{0.8}Zr_{0.2}O_2$ system.[20] These contrasting observations may arise from the use of different "non-innocent" supports. To elucidate the intrinsic effect of the metal dopants on Ni-based methanation catalyst, it is therefore essential to employ an inert support.

Herein, a series of Ni-M/SiO_2 (M = Mn, Co, Cu) bimetallic catalysts was prepared via an ethylene glycol-assisted sol-gel method, which was recently demonstrated to yield finely dispersed Ni nanoparticles embedded within a mesoporous silica matrix.[21] Cu doping was found to be detrimental, resulting in a pronounced decrease in activity for Ni–Cu/SiO_2 compared with pristine Ni/SiO_2. In contrast, the incorporation of Mn or Co enhanced the CO_2 methanation performance of the Ni/SiO_2 catalyst. Specifically, the Mn-doped catalyst exhibited high activity at relatively low temperatures (below

250 °C), whereas Co addition markedly improved catalytic performance at higher temperatures (above 300 °C). Through a combination of complementary characterization techniques, we elucidate the effects of metal doping on (i) the physicochemical properties of the catalysts and (ii) the CO_2 methanation mechanism.

2. Experimental section

2.1. Catalyst preparation.

The bimetallic Ni-M/SiO_2 (M = Mn, Co, and Cu) and a monometallic Ni/SiO_2 were both prepared by a sol-gel method (Scheme 1). Typically, anhydrous ethanol (EtOH), distilled H_2O, and HNO_3 were added to tetraethyl orthosilicate (TEOS) at a molar ratio of 3:1.8:0.03:1 and stirred for 1 h to obtain a clear SiO_2 sol. The required amount of $Ni(NO_3)_2 \cdot 6H_2O$ and transition metals (Mn, Co, and Cu) nitrates were dissolved in ethylene glycol (EG) and methanol (V_{EG}:$V_{methanol}$ = 3:2), and the solution was maintained at 2 M of metal salts (Ni + dopant). The solution was then added to the SiO_2 sol and stirred for another 1 h. The obtained slurry was aged at 30 °C for 12 h and dried at 120 °C for another 12 h to form a gel. The dried gel was calcined in air at 300 °C (1 °C/min) for 2 h, and then at 500 °C (1 °C/min) for an additional 2 h. The mass fraction of nickel loading was fixed at 20% for all the catalysts and the theoretical molar ratio for Ni/M (M = Mn, Co, and Cu) was fixed at 4. The calcined samples were denoted as "NiO-M/SiO_2". The calcined catalyst was reduced in situ in the reactor under a H_2/He flow (see below), and the corresponding samples were denoted "Ni-M/SiO_2". Note that the word "bimetallic" is here simply used to denote the fact that the formulation contains 2 metals (not to affirm that bimetallic alloys are formed).

2.2. Characterization.

N_2 adsorption-desorption analyses were carried out on a Tristar 3000 (Micromeritics, USA) instrument. The sample was degassed at 250 °C for 3 h to remove physically adsorbed water and impurities on the surface before the measurement. The total pore volume (V_p) was calculated from the amount of nitrogen absorbed at a P/P_0 of 0.98 and the pore size distribution of each catalyst was drawn from the desorption branch of the isotherm using the Barrett-Joyner-Halenda (BJH) method.

X-ray diffraction (XRD) analyses were carried out by means of a Bruker D8 Advance diffractometer (Bragg–Brentano geometry) on both reduced and spent catalysts. The diffractometer works with a Cu Kα source (λ=0.15418 nm) at 1200 W (30 mA, 40 kV). For the reduced samples, the catalysts were cooled to room temperature under flowing inert gas after the reduction treatment. The samples were then promptly transferred to the diffractometer and measured immediately, minimizing their exposure to ambient air. Diffraction patterns have been acquired by setting the following parameters: 2θ range 10°-80°, step size 0.05° (2θ) and 1.5 s each step.

H_2 chemisorption at 30 °C was used to measure the Ni dispersion using the ASAP 2010C apparatus from Micrometrics. The catalyst (200 mg) was loaded into a Pyrex tube, and subsequently degassed at room temperature in He for 30 min. After evacuation, the sample was reduced in pure H_2 at 500 °C for 2 h, following the same in

situ reduction procedure applied prior to catalytic methanation tests (Section 2.3). After reduction, the catalyst was purged with He for 1 h at the same temperature and subsequently cooled to 30 °C under inert atmosphere. Two H_2 adsorption isotherms were recorded in the pressure range of 0.13–60 kPa. The first isotherm represents the total hydrogen uptake, including both reversible physisorption and irreversible chemisorption. The sample was then evacuated at 30 °C to remove reversibly adsorbed hydrogen. A second isotherm was measured under identical conditions, corresponding exclusively to reversible adsorption. The subtraction of the linear part of the two isotherms gave the total amount of irreversibly chemisorbed H_2. The amount of surface Ni atoms was calculated from the amount of chemisorbed H_2 and the Ni loading, assuming that the chemisorption stoichiometry is H:Ni = 1 and neglecting any contribution of the dopant.

Transmission electron microscopy (TEM) was performed using JEOL-2100 Plus (LaB6) equipped with an Oxford EDX detector. The catalyst powder was added in ethanol and ultrasonically dispersed for 15 min. A few drops of the suspension was then deposited onto the copper grid. The statistical nickel particle sizes of samples were obtained by Nano Measurer software. For each sample, 30 Ni particles were counted to determine the mean particle size.

Xay photoelectron spectroscopy (XPS) experiments were carried out using an SSX 100/206 spectrometer (Surface Science Instruments, USA) with Al Kα radiation operated at 10 kV and 20 mA. The binding energy scale was calibrated on the Si 2p peak, fixed at 103.5 eV.[22]

H_2-temperature programmed reduction (H_2-TPR) and CO_2 temperature-programmed desorption (CO_2-TPD) measurements were performed on a Hiden Autochem II 2920 instrument with an on-line QIC20 mass spectrometer (MS). For the H_2-TPR, the sample (50 mg) was pretreated in a high purity Ar flow (20 mL/min) at 350 °C for 0.5 h to remove water and other contaminants. Then the sample was cooled down to 30 °C , and a 5% H_2/Ar flow (20 mL/min) was introduced into the system. The MS signal and sample temperature were recorded while the temperature was increased to 900 °C at a heating rate of 10 °C/min. For the CO_2-TPD, 50 mg sample was reduced in-situ at 500 °C for 2 h in a 5% H_2/Ar flow (20 mL/min). After reduction, the sample was purged in an Ar flow (20 mL/min) for 1 h. Then the sample was cooled down to 50 °C, and a 15% CO_2/Ar flow (20 mL/min) was admitted for 1 h. The system was then purged by an Ar flow (20 mL/min) for 1 h at 50 °C. Finally, the catalyst was heated up to 900 °C at a rate of 10 °C /min in the same Ar flow.

In-situ diffuse reflectance infrared Fourier transform spectroscopy (DRIFTS) of CO_2 methanation was carried out on a Nicolet 6700 spectrometer. For each DRIFTS measurement, the catalyst was mixed with KBr (1:5 mass ratio) and 0.03 g of this mix was loaded into the chamber and in-situ reduced at 500 °C for 1 h by a 50% H_2/50% He (20 mL min^{-1}). Then, the gas was changed to He to flush the sample for 30 min at 500 °C to remove residual H_2. Afterwards, the temperature was lowered to 30 °C and then the background was recorded. Subsequently, a CO_2/H_2/He mixture gas (6.7%

CO_2/26.8% H_2/66.5% He at a flow 15 mL min^{-1}) was introduced and the temperature was increased in a step mode from 100 to 400 °C with an increment of 50 °C, while the spectra were collected at each temperature when reaching a steady state.

Temperature programmed surface reaction of CO_2 and H_2 (CO_2+H_2 TPSR) experiment was performed on a Hiden Autochem II 2920 instrument with an on-line QIC20 mass spectrometer (MS). 50 mg of catalyst was reduced in-situ at 500 °C for 2 h under a 5% H_2/Ar flow (20 mL/min) and then was purged in an Ar flow (20 mL/min) for 1 h. After cooling down to 50 °C under Ar (20 ml/min), a 20 mL/min flow of 15% CO_2/Ar was introduced to the reactor for 1 h and purged by Ar gas for 30 min. The TPSR profiles were recorded from 50 °C to 650 °C with a 5 °C/min heating rate when 5 mL/min of 5% H_2/Ar was flowed into the reactor. The signal of CH_4 and CO_2 was examined by MS with the m/z of 15 and 44. For the formaldehyde-temperature programmed surface reaction (HCHO-TPSR) test, 50 mg of reduced catalyst was placed into the reactor and then the reactor was immersed in a HCHO solution (Sigma-Aldrich, 37 wt. % in H_2O, containing 10-15% methanol as stabilizer) for 1 h. After installing the reactor, 20 mL/min of Ar was introduced to the reactor for 30 min. The TPSR profiles were recorded from 30 °C to 250 °C with a 5 °C/min heating rate when 5 mL/min of 5% H_2/Ar was flowed into the reactor. The signal of HCHO and methanol was examined by MS with the m/z of 29 and 31.

2.3. CO_2 methanation.

Catalytic performance was measured in a continuous flow gas-phase microreactor, at atmospheric pressure, as described before.[21] 50 mg of catalyst was placed in the reactor and reduced in situ at 500 °C for 2 h in a 50% H_2/50% He flow (40 mL/min) and then cooled down to 200 °C. Then, a mixture of 10% CO_2 and 40% H_2 balanced with He was introduced to the reactor. The total gas flow rate was 20 mL/min with a GHSV of 24,000 mL g^{-1} h^{-1}. The catalytic tests were carried out in step mode between 200 °C and 400 °C. Each temperature was maintained for 88 min, allowing for 4 GC analyses. The gas exiting the reactor was analyzed on a gas chromatograph (Varian CP3800), equipped with Hayesep Q, Molsieve 5A, and CP-Sil-5CB columns. The separated gases were analyzed with a flame ionization detector (CH_4) and a thermal conductivity detector (CO and CO_2). All transfer lines were maintained at 125 °C to avoid water condensation. Conversion (X_{CO2}) and selectivity (S_{CH4}) were calculated according to the following equations:

$$X_{CO2} = \frac{F_{CO_2,in} - F_{CO_2,out}}{F_{CO_2,in}} \qquad (1)$$

$$S_{CH4} = \frac{F_{CH_4,out}}{F_{CO_2,in} - F_{CO_2,out}} \qquad (2)$$

where F is the molar flow rate. In order to verify there are no heat and mass transfer limitations in the tested conditions, we did an extra experiment by varying the amount of catalyst and flow and changing the size of the catalyst pellets (see supplementary information, Fig. S1).

The turnover frequency (TOF) was calculated by the following equation:

$$\text{TOF } (s^{-1}) = \frac{X_{CO2} \times F_{CO2,in}}{\text{moles of surface Ni atoms}} \qquad (3)$$

It is noted that for the TOF calculation, the CO_2 conversion is kept below 15%, where the effect of heat and mass transfer is negligible, and moles of surface Ni atoms was determined based on H_2 chemisorption.

3. Results and discussion.

3.1. Catalytic performance.

The CO_2 methanation performance of Ni/SiO_2 and bimetallic $Ni\text{-}M/SiO_2$ catalysts was evaluated in the 200-400 °C temperature range at a GHSV of 24000 mL g^{-1} h^{-1}. The CO_2 conversion and CH_4 selectivity are shown in Fig. 1. In terms of CH_4 selectivity, the Ni/SiO_2 catalyst exhibited values above 90% at temperatures ≥ 250 °C. The addition of Mn and Co exerted little influence on CH_4 selectivity, whereas Cu addition led to increased CO formation over $Ni\text{-}Cu/SiO_2$ via the reverse water gas shift (RWGS) reaction ($CO_2 + H_2 \rightarrow CO + H_2O$), resulting in CH_4 selectivity below 90% across the entire temperature range. The CO selectivity is presented in Fig. S2b. The results confirm that the reduced CH_4 selectivity of the Cu-doped catalyst originates from increased CO formation via the RWGS reaction. In contrast, Mn- and Co-doped catalysts maintained high CH_4 selectivity with low CO formation, consistent with their superior methanation performance. Both Mn and Co addition enhanced CO_2 conversion (and CH_4 yield) in the whole temperature range. Notably, Mn addition had a more pronounced effect at low temperature (≤ 250 °C), while Co addition had a more pronounced effect at high temperature (≥ 300 °C). On the contrary, Cu addition consistently exerted a detrimental effect on catalytic activity. Turnover frequency (TOF) values for CO_2 conversion were also calculated (Table 1, the corresponding CO_2 conversion tested at high GHSV is listed in Table S1). At both 250 °C and 300 °C, $Ni\text{-}Mn/SiO_2$ and $Ni\text{-}Co/SiO_2$ exhibited higher TOF values than Ni/SiO_2, while $Ni\text{-}Cu/SiO_2$ showed lower TOF values. Specifically, at 250 °C, the TOF of $Ni\text{-}Mn/SiO_2$ (0.026 s^{-1}) is 1.53 times higher than that of $Ni\text{-}Co/SiO_2$ (0.017 s^{-1}). Conversely, at 300 °C, the TOF of $Ni\text{-}Co/SiO_2$ (0.102 s^{-1}) is 1.40 times higher than that of $Ni\text{-}Mn/SiO_2$ (0.073 s^{-1}). A comparison with reported Ni-based catalysts is also provided in Table 1. Although Ni catalysts supported on non-reducible oxides (e.g., SiO_2, Al_2O_3, etc.) generally exhibit lower TOF values than those supported on reducible oxides (e.g., CeO_2, ZrO_2, etc.), a notable enhancement in TOF was observed for $Ni\text{-}Mn/SiO_2$ at 250 °C and $Ni\text{-}Co/SiO_2$ at 300 °C. While the determination of activation energies could provide additional insight into the nature of the catalytically active centers, these dedicated measurements (at low conversion) were not performed in the present study. Future work could explore activation energy determinations to further elucidate the effect of metal dopants on the reaction kinetics.

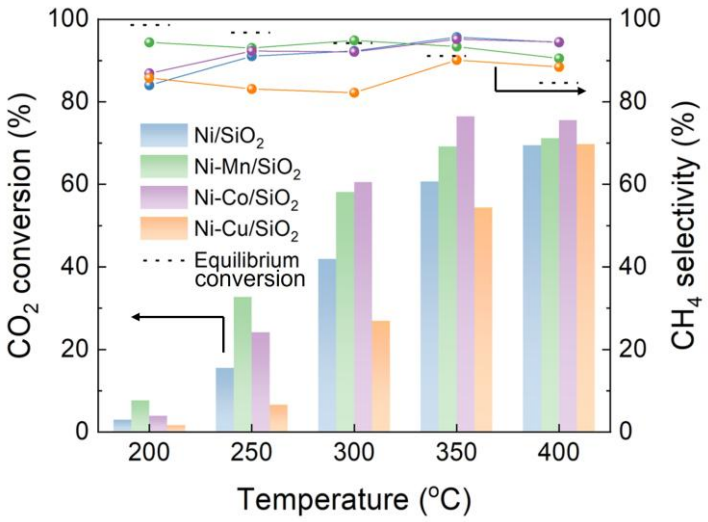

Fig. 1. CO_2 methanation performance showing CO_2 conversion (bars) and CH_4 selectivity (lines) as a function of temperature. Reaction conditions: 10% CO_2, 40% H_2, balance He; total flow rate 20 mL min^{-1} (GHSV = 24,000 mL g^{-1} h^{-1}). The Ni/SiO_2 catalyst showed good repeatability (Fig. S2a).

Table 1. The comparison of TOF values towards CO_2 conversion of the reported Ni catalysts for CO_2 methanation

Catalyst	Preparation method	T (°C)	TOF (s^{-1})	Ref.
Ni/SiO_2	Sol-gel	250	0.009	This work
$Ni\text{-}Mn/SiO_2$			0.026	
$Ni\text{-}Co/SiO_2$			0.017	
$Ni\text{-}Cu/SiO_2$			0.004	
Ni/SiO_2		300	0.036	
$Ni\text{-}Mn/SiO_2$			0.073	
$Ni\text{-}Co/SiO_2$			0.102	
$Ni\text{-}Cu/SiO_2$			0.021	
50 Ni/SiO_2	Sol-gel	250	0.016	[21]
50 Ni/SiO_2-IM	Impregnation	250	0.006	[21]
Ni/Al_2O_3	Incipient wet impregnation	250	~0.02	[23]
Ni/ZSM-5	Wet impregnation	250	0.008	[24]
Ni/SBA-15-WI	Impregnation	250	0.012	[25]
Ni/SBA-15-AE	Ammonia evaporation	250	0.016	[25]
Ni/Y_2O_3-HN	Hydrothermal treatment and impregnation	225	0.009	[26]
$Ni/mpCeO_2$	Strong electrostatic adsorption	225	0.183	[6]
Ni/ZrO_2-P	Plasma decomposition	235	0.071	[10]

3.2. Catalyst characterization.

3.2.1. Transmission electron microscopy (TEM)

The catalyst morphology and nanostructure were investigated by TEM. As shown in Fig. 2a-d, uniformly dispersed nanoparticles were observed for all reduced catalysts. The average Ni particle size was estimated from TEM micrographs (Fig. S3). As listed in Table 1, the average particle size of Ni/SiO_2, $Ni\text{-}Mn/SiO_2$, $Ni\text{-}Co/SiO_2$, and $Ni\text{-}Cu/SiO_2$ were 3.3, 4.7, 3.8 and 3.5 nm, respectively. The lattice fringe spacing observed for Ni/SiO_2 is 0.203 nm, corresponding to the Ni (111) plane.[6] The presence of the

Ni (111) plane was also confirmed for Ni-Mn/SiO_2 and Ni-Cu/ In contrast, for Ni-Co/SiO_2, an interplanar spacing of 0.216 nm was observed, which can be assigned to the NiCo (1-11) plane, indicating the formation of NiCo alloy.[27] Furthermore, Mn_3O_4 (312) plane over Ni-Mn/SiO_2, CoO (200) plane over Ni-Co/SiO_2 and Cu (111) plane over Ni-Cu/SiO_2 are confirmed by the observation of 0.174 nm, 0.236 nm, and 0.218 nm lattice fringe distances, respectively.[28-30]

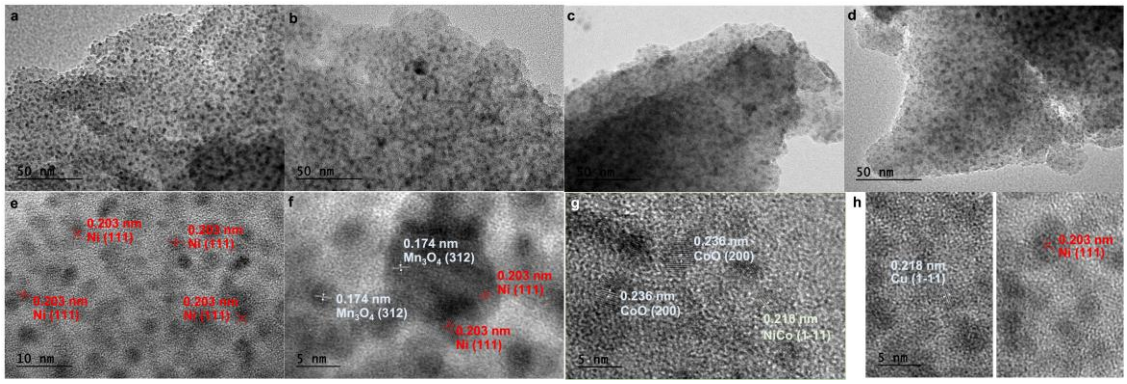

Fig. 2. TEM images of (a, e) Ni/SiO_2, (b, f) Ni-Mn/SiO_2, (c, g) Ni-Co/SiO_2, and (d, h) Ni-Cu/SiO_2 catalysts.

3.2.2. N_2 physisorption

The catalysts textural properties were characterized by N_2 physisorption. As shown in Fig. S4, all catalysts exhibited type IV adsorption isotherms with a H1-type hysteresis loop, characteristic of mesoporous materials.[31] The average pore diameter were within a narrow range of 2.1–2.4 nm (Table 2). Specific surface area and total pore volume were comparable for all samples, reaching 510-570 m^2/g and 0.15-0.19 $cm^3\ g^{-1}$, respectively.

Table. 2. Physical properties of the prepared catalysts.

Sample	S_{BET} (m^2/g)	V_p (cm^3/g)	D_p (nm)	Ni content[a] (%)	Dopant content[a] (%)	Ni particle size[b] (nm)	Dispersion[c] (%)
Ni/SiO_2	510	0.15	2.1	18.9	-	3.3	15.8
Ni-Mn/SiO_2	539	0.19	2.4	18.3	5.1	4.7	12.4
Ni-Co/SiO_2	564	0.16	2.2	18.2	4.7	3.8	13.4
Ni-Cu/SiO_2	566	0.14	2.2	18.7	4.6	3.5	14.1

[a] Determined by ICP-AES measurement.

[b] Obtained from the TEM results.

[c] Determined by H_2 chemisorption.

3.2.3. X-ray Diffraction (XRD)

The crystalline structures of the catalysts were analyzed by XRD (Fig. S5). All samples exhibited a broad diffraction signal centered at 2θ ~23°, which is ascribed to the amorphous silica matrix.[32] For the calcined samples, two weak and broad diffraction reflections at 37.1° and 43.2° were assigned to the (111) and (200) planes of NiO.[6] After reduction under H_2, no obvious diffraction reflections were detected for the reduced samples, indicating that the expectedly formed Ni particles were highly dispersed and of small size. Consistently, a high Ni dispersion value (15.8%) was determined by H_2 chemisorption measurement for Ni/SiO_2. For the metal-doped catalysts, the Ni dispersion values remained within the similar range but were slightly lower (listed in Table 1), suggesting the presence of marginally larger Ni particles.

3.2.4. H_2 temperature-programmed reduction (H_2-TPR)

The reduction behavior of calcined catalysts was investigated using H_2-TPR measurements (Fig. 3). Two H_2 consumption peaks centered at 373 °C and 565 °C were fitted for NiO/SiO_2 catalysts, which correspond to the reduction of Ni^{2+} to metallic Ni^0, with the contribution at higher temperature associated to NiO particles in stronger interaction with the SiO_2 matrix. The addition of Mn, Co, or Cu facilitated the reduction of Ni species, as indicated by a shift of the NiO reduction peaks to lower temperatures compared to the pristine Ni/SiO_2 catalyst. For $NiO\text{-}Co/SiO_2$, an additional high-temperature peak at 740 °C is assigned primarily to the reduction of Co oxides.[33, 34] TEM analyses indicate the formation of NiCo alloy after reduction at 500 °C, suggesting that the reduction of Ni and Co species may partially overlap with alloy formation. For $NiO\text{-}Cu/SiO_2$, a distinct low-temperature peak at 257 °C is attributed to the reduction of Cu^{2+} to metallic Cu, which occurs before NiO reduction.[35] A distinct reduction of Mn oxide was not observed for $NiO\text{-}Mn/SiO_2$, likely due to overlap with the NiO reduction peaks or the higher reduction temperature of MnO_x species.

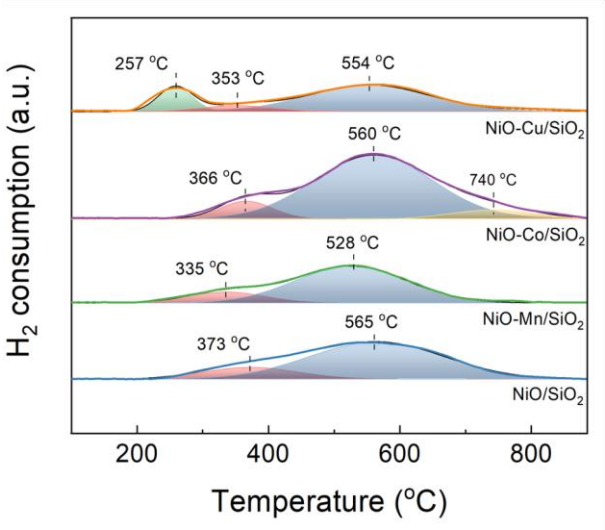

Fig. 3. H_2-TPR profiles of the calcined catalysts.

3.2.5. X-ray photoelectron spectroscopy (XPS)

The chemical state and surface compositions of the reduced catalysts were analyzed by XPS. As shown in the Ni $2p_{3/2}$ spectra (Fig. 4a), the peak at 852.6 eV observed for all reduced catalysts confirms the presence of metallic Ni.[36] Furthermore, the peak at 855.7 eV with a broad satellite at 861.7 eV is attributed to the presence of NiO, which can be explained by the re-oxidation of the surface of small Ni nanoparticles upon exposure to ambient air, rather than reflecting bulk unreduced NiO.[37] This is supported by the high catalytic activity of the reduced samples and TEM observations showing predominantly metallic Ni particles. The chemical state of the promoters (Mn, Co, and Cu) was also examined (Fig. 4b). The spectrum of Mn $2p_{3/2}$ of Ni-Mn/SiO_2 can be deconvoluted into three peaks with binding energies of 644.7 eV, 641.3 eV, and 639.8 eV, corresponding to Mn^{4+}, Mn^{3+} and Mn^{2+}, respectively.[38, 39] In the spectrum of Co $2p_{3/2}$ of Ni-Co/SiO_2, the peak at 782.1 eV accompanied by a broad satellite peak at 786.8 eV are attributed to surface Co^{2+} species, and the weak shoulder peak at around 776.9 eV can be attributed to the presence of Co^0 species.[40] Compared with the calcined catalysts (NiO-Mn/SiO_2 and NiO-Co/SiO_2, see Fig. S6), the reduced samples exhibit somewhat more reduced Mn and Co species. Nevertheless, oxidized dopant species (Mn^{4+}/Mn^{3+} and Co^{2+}) remain the major surface species. This observation is consistent with the absence of a distinct reduction peak for the NiO-Mn/SiO_2 and NiO-Co/SiO_2 catalysts in H_2-TPR profiles. On the contrary, the Cu $2p_{3/2}$ spectrum of Ni-Cu/SiO_2 shows only a single peak at around 933.0 eV, attributed to Cu^0 species.[41] Therefore, the partially oxidized Cu found in NiO-Cu/SiO_2 (Fig. S6) is fully reduced to metallic Cu upon reduction, consistent with the additional reduction peak detected for the NiO-Cu/SiO_2 catalyst in H_2-TPR analysis.

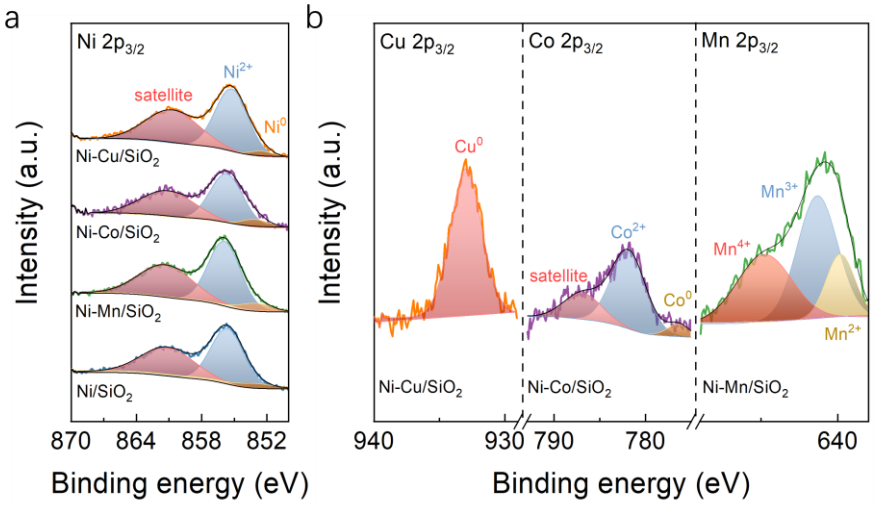

Fig. 4. XPS spectra of (a) Ni $2p_{3/2}$, (b) Mn $2p_{3/2}$, Co $2p_{3/2}$, and Cu $2p_{3/2}$ over the prepared catalysts.

3.2.6. CO_2 Temperature-Programmed Desorption (CO_2-TPD)

CO_2-TPD experiments were performed to characterize the surface basicity (Fig. 5). CO_2 desorption events – characterized by their intensity and temperature – can reveal the amount and strength of different CO_2 adsorption sites. The desorption peak at

approximately 100 °C is attributed to physisorbed CO_2.[42, 43] Furthermore, three distinct desorption peaks were observed at higher temperature (ca. 150 °C, ca. 205 °C, and over 550 °C), corresponding to three kinds of adsorbed CO_2 species over the weak, medium and strong basic site, which exist in the form of bicarbonate, monodentate carbonate and bidentate carbonate species.[6] Previous studies have indicated that the catalytic activity can be promoted by increasing the number of weak and medium basic sites but is not correlated with the strong basic sites, which are thought to suppress further hydrogenation.[44, 45] The amount of CO_2 adsorption at weak and medium basic sites is summarized in Table 3. It can be seen that Ni-Cu/SiO_2 exhibited higher weak and medium basicity than Ni/SiO_2, while Ni-Mn/SiO_2 and Ni-Co/SiO_2 showed much lower weak and medium basicity than Ni/SiO_2.

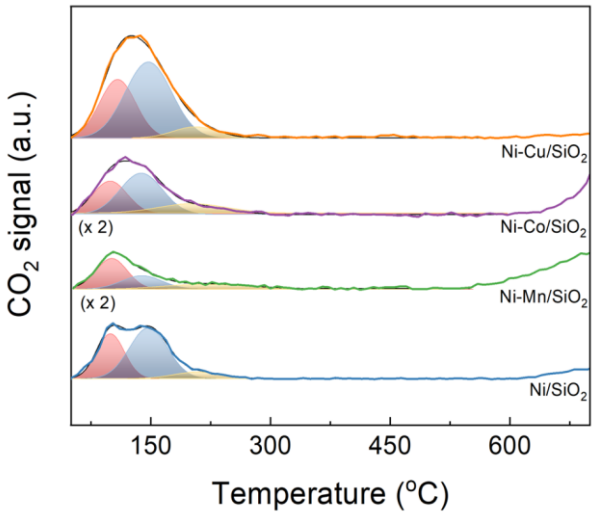

Fig. 5. CO_2-TPD profiles of the prepared catalysts.

Table 3. CO_2-TPD analyses of the prepared catalysts. Values correspond to the integrated CO_2 desorption peak area (arbitrary units, a.u.) under identical experimental conditions.

	Weak basicity	Medium basicity
Ni/SiO_2	3.29	0.55
Ni-Mn/SiO_2	0.45	0.35
Ni-Co/SiO_2	1.45	0.54
Ni-Cu/SiO_2	5.97	0.82

Particle size, reducibility, and surface basicity are widely recognized as key factors governing catalytic performance.[46] In the present study, Ni-Cu/SiO_2 exhibited (i) comparable Ni dispersion (H_2 chemisorption), (ii) enhanced reducibility (H_2-TPR), and (iii) increased surface basicity (CO_2-TPD) relative to Ni/SiO_2. Based on these

characteristics, one would expect equal or superior catalytic performance; however, Ni–Cu/SiO_2 displayed lower activity than Ni/SiO_2. The addition of Mn and Co led to comparable dispersion (average particles size of 3.3 and 4.7 respectively) in comparison to Ni/SiO_2 (3.5 nm). It should be noted that the reaction is strongly structure-sensitive.[47, 48] It was reported that the CH_4 formation rate over Ni/SiO_2 catalyst reaches a maximum at 3.9 nm and decreases for smaller and bigger Ni particles.[47] Therefore, slight variations in particle size may influence activity—for instance, Mn-doped catalysts with Ni particles significantly larger than 3.9 nm might be expected to exhibit lower activity than the pristine Ni catalyst. Mn- and Co-doped catalysts show enhanced reducibility, and lower basicity in comparison to Ni/SiO_2. The latter effect might be anticipated to adversely impact catalytic performance. However, a higher catalytic performance was obtained for the Ni-Mn/SiO_2 and Ni-Co/SiO_2 than Ni/SiO_2.

Overall, these observations suggest the presence of an additional factor that significantly influences CO_2 methanation activity in this catalyst system. To rationalize this apparent discrepancy, we propose to investigate the reaction mechanism as it occurs on the different catalysts.

3.3. Investigation of the CO_2 methanation mechanism by in situ DRIFTS and TPSR experiments.

In general, the possible CO_2 methanation reaction pathways can be divided into three categories: the formate pathway, the RWGS+CO-hydrogenation pathway and the direct C−O bond cleavage pathway.[46] In this study, in-situ DRIFTS and TPSR experiments were carried out in a reacting mixture of CO_2/H_2, in an attempt to identify the surface species that form during reaction and thereby enhance our understanding of the possible CO_2 methanation pathways over the studied catalysts.

Fig. 6 shows the DRIFT spectra recorded under CO_2 methanation conditions over the four catalysts, from 100 °C to 400 °C. For Ni/SiO_2 (Fig. 6a), two primary types of surface species are observed at 100 °C: carbonates and carbonyls. In detail, monodentate carbonate (1512 cm^{-1}), bidentate carbonate (1462 cm^{-1}) and bicarbonate (1388 cm^{-1}) can be observed.[49] The presence of these carbonates as the CO_2-derived surface species is consistent with CO_2-TPD results. As the temperature increases, the intensity of the carbonate bands decreases, with the bicarbonate peak disappearing completely at 250 °C. Meanwhile, bands attributed to monodentate formates (1330 cm^{-1}) and bidentate formates (1369 cm^{-1})[6] emerge with high intensity at 150 °C and 250 °C respectively. These formate species are believed to originate from the hydrogenation of monodentate and bidentate carbonates.[45] In addition to carbonate and formate species, 2-fold carbonyl (1947 cm^{-1}) and 3-fold carbonyl (1833 cm^{-1})[6] species are observed from 100 °C. These carbonyl species adsorbed on Ni sites are thought to originate from the dissociative adsorption of CO_2.[50] The adsorbed carbonyl species can further react with the adsorbed H atoms on Ni sites to produce formyl (*HCO) species, as indicated by the band at 1747 cm^{-1}[51], and the formyl species can be subsequently hydrogenated towards CH_4. Furthermore, formaldehyde

species (1123 cm^{-1}) and methoxy species (1044 cm^{-1}) are also detected as intermediates during the reaction.[51, 52]

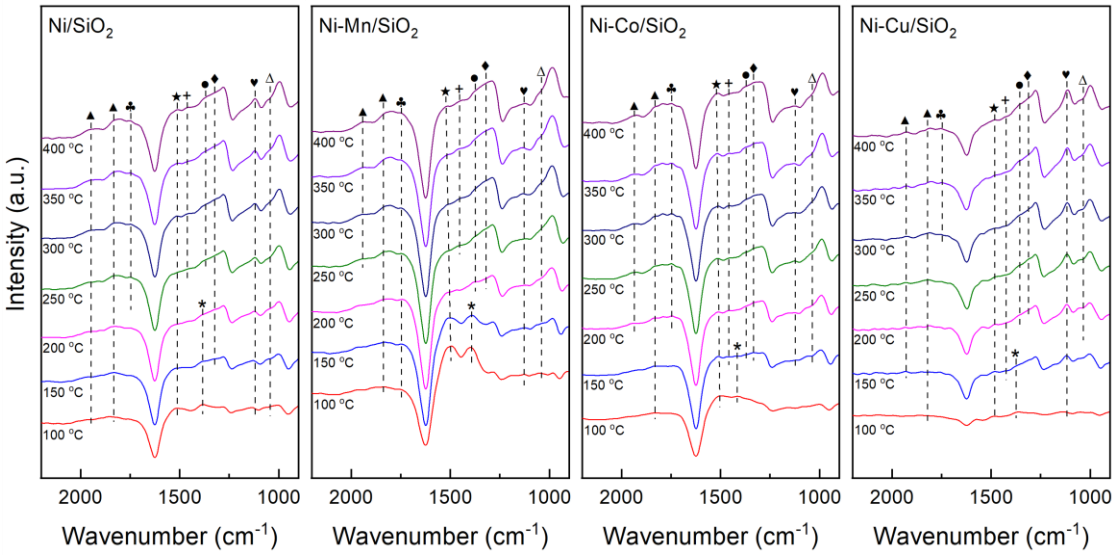

Fig. 6. CO_2 methanation DRIFTS experiments on the prepared catalysts. Symbol definition: carbonyl (▲), formyl (♣), monodentate carbonate (★), bidentate carbonate (+), bicarbonate (*), bidentate formate (●), monodentate formate (♦), formaldehyde (♥), and methoxy (Δ).

For the bimetallic Ni-M/SiO_2 catalysts, carbonate and carbonyl species were observed with higher intensity on Ni-Mn/SiO_2, Ni-Co/SiO_2, and lower intensity on Ni-Cu/SiO_2, compared with Ni/SiO_2. Furthermore, the intensities of formate and formaldehyde intermediates differ markedly among the four catalysts. Specifically, the intensity of the formate species follows the sequence: Ni-Cu/SiO_2 < Ni/SiO_2 < Ni-Mn/SiO_2 < Ni-Co/SiO_2 (Fig. 7a), whereas the intensity of the formaldehyde species follows the sequence: Ni-Mn/SiO_2 < Ni-Co/SiO_2 < Ni/SiO_2 < Ni-Cu/SiO_2 (Fig. 7b).

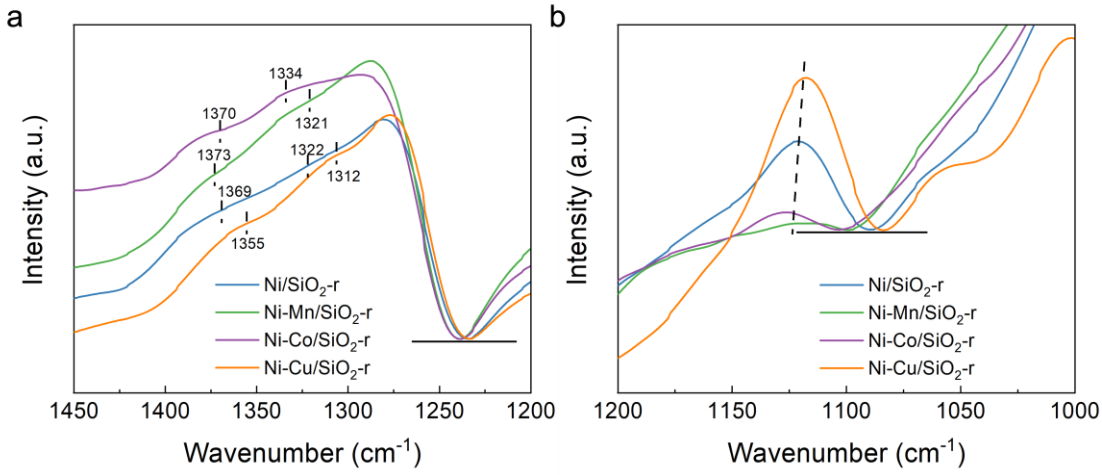

Fig. 7. Comparison of peak intensity of (a) formate intermediate and (b) formaldehyde intermediate.

Monodentate carbonate species can be hydrogenated to CH_4 via the formate pathway, in which the formate formation is the rate determining step [21]. Carbonyl species generated from the dissociation of CO_2 on the catalyst surface is hydrogenated to CH_4 via the RWGS+CO hydrogenation pathway, where the rate determining step is proposed to be the formation of methoxy from formaldehyde.[21] In this context, the DRIFTS results indicate that the formation of formate is promoted by Mn and Co addition, as indicated by the higher peak intensity of formate over Ni-Co/SiO_2 and Ni-Mn/SiO_2 compared with Ni/SiO_2 (Ni-Co/SiO_2 > Ni-Mn/SiO_2 > Ni/SiO_2). These observations suggest that Mn and Co facilitate the formate pathway, with Co exerting a more pronounced effect.

Mn and Co addition appear to facilitate the formation of methoxy from formaldehyde as suggested by the lower peak intensity of formaldehyde over Ni-Mn/SiO_2 and Ni-Co/SiO_2 compared with Ni/SiO_2 (Ni-Mn/SiO_2 < Ni-Co/SiO_2 < Ni/SiO_2). This suggests that Mn and Co promote the RWGS–CO hydrogenation pathway, with Mn exhibiting a stronger effect. To further investigate the effect of dopants on the transformation of formaldehyde, HCHO-TPSR experiments were conducted. In Fig. 8a, the m/z = 29 signal corresponds to formaldehyde desorption, and the m/z = 31 signal corresponds to methanol desorption (methanol is present as a stabilizer in the HCHO solution). Each of these signals displays a single desorption peak. The curve of m/z = 15, however, shows two distinct desorption peaks. m/z = 15 could represent both methanol and methane. Since m/z = 15 can correspond to both methanol and methane, the first peak, which follows the same trend as the m/z = 31 methanol signal, is attributed to methanol desorption. The second peak is therefore assigned to CH_4 formation. Similar trends were observed for the three bimetallic catalysts (Fig. S7). Fig. 8b compares the m/z = 15 profiles of all four catalysts. The Ni/SiO_2, Ni-Mn/SiO_2, Ni-Co/SiO_2, and Ni-Cu/SiO_2 catalysts exhibit CH_4 formation breakthroughs temperatures at 167 °C, 160 °C, 162 °C, and 181 °C, respectively, with maximum CH_4 production at 206 °C, 197 °C, 201 °C, and 240 °C, respectively. The lower breakthrough and maximum temperatures for Ni–Mn/SiO_2 and Ni–Co/SiO_2 indicate that these catalysts are intrinsically more active than Ni/SiO_2 for the hydrogenation of formaldehyde to CH_4, with Mn exhibiting a slightly stronger promoting effect than Co. In contrast, Cu addition appears to inhibit the hydrogenation of formaldehyde to CH_4.

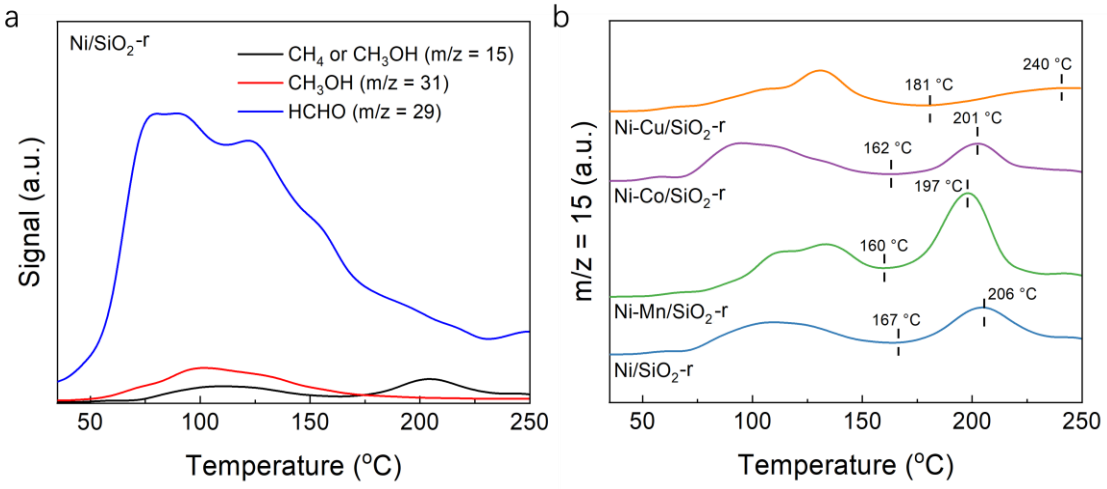

Fig. 8. (a) The curves of m/z = 15, 29, and 31 in HCHO-TPSR over Ni/SiO_2. (b) The curve of m/z = 15 in HCHO-TPSR over the reduced catalysts.

Although it should be noted that energy barriers are facet-dependent,[53], our calculations made on the Ni (111) facet led us to consider that the rate determining step of the RWGS+CO hydrogenation pathway has a lower energy barrier than that of the formate pathway.[21] The stronger promotion effect of Mn on the hydrogenation of formaldehyde to CH_4 (the rate determining step of RWGS+CO hydrogenation pathway) is revealed by the highest activity of $Ni\text{-}Mn/SiO_2$ at low temperature (≤ 250 °C). At higher temperatures (> 300 °C), $Ni\text{-}Co/SiO_2$ catalyst exhibits highest activity, as Co maximally facilitates the formation of formate species, which is the rate-determining step of the formate pathway. On the contrary, Cu addition suppresses both the formation of formate and the transformation of formaldehyde to methoxy, resulting in lower activity for $Ni\text{-}Cu/SiO_2$ compared with Ni/SiO_2.

CO_2+H_2 TPSR tests were also carried out to explore how CO_2 molecules dynamically interact with the catalysts surface during CH_4 production. Specifically, CO_2 was first adsorbed on the catalyst and then exposed to a H_2 atmosphere while the temperature gradually increased. As shown in Fig. 9, the total amount of CH_4 formed over the prepared catalysts decreases in the order: $Ni\text{-}Cu/SiO_2$ > Ni/SiO_2 > $Ni\text{-}Co/SiO_2$ > $Ni\text{-}Mn/SiO_2$, which is consistent with the amount of adsorbed CO_2 measured in CO_2-TPD experiments (i.e. with total basicity). After deconvoluting the profiles, three CH_4 formation peaks can be identified for all the prepared catalysts. Based on a previous mechanistic study[21], we propose to assign peaks α, β, and γ (Fig. 9) to the CH_4 formed via the RWGS+CO hydrogenation pathway, formate pathway, and C-O cleavage pathway, respectively. For $Ni\text{-}Mn/SiO_2$, the α peak shifts to lower temperature, indicating that Mn addition facilitates the CH_4 formation via the RWGS+CO hydrogenation pathway. For $Ni\text{-}Co/SiO_2$, the α peak is unaffected but the β peak shifts to lower temperature, suggesting that Co addition facilitates the CH_4 formation via the formate pathway. On the contrary, both the α and the β peaks shift to higher temperatures for $Ni\text{-}Cu/SiO_2$, indicating the Cu addition inhibits the CH_4 formation via the RWGS+CO hydrogenation and formate pathway.

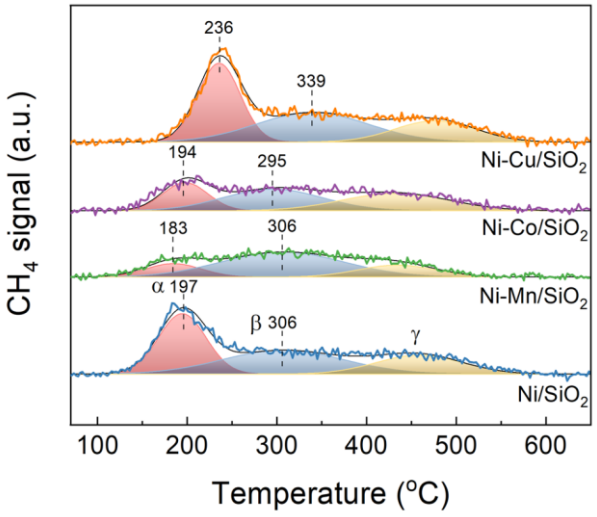

Fig. 9. TPSR over reduced catalysts.

Based on in-situ DRIFTS and TPSR results, the promoting effects of Mn and Co addition can be identified. RWGS+CO hydrogenation pathway is dominant at low temperature (below 250 °C). Mn addition facilitates the RWGS+CO hydrogenation pathway to the greatest extent, which leads to the highest activity of Ni-Mn/SiO_2 at low temperature. The formate pathway can proceed in parallel but is more important at higher temperature (above 300 °C), where Co addition maximally promotes formate formation, leading to the highest activity of Ni-Co/SiO_2. Cu addition suppresses both pathways, resulting in the lowest activity for Ni-Cu/SiO_2.

4. Conclusion

In summary, a series of bimetallic Ni-M/SiO_2 mesoporous catalysts (M = Mn, Co, and Cu) were synthesized by sol-gel method and used for the CO_2 methanation reaction. Ni-Mn/SiO_2 and Ni-Co/SiO_2 show higher activity, while Ni-Cu/SiO_2 shows lower activity than the pristine, unpromoted, Ni/SiO_2 catalyst. The effect of doping on dispersion, reducibility and basicity do not seem to explain the activity trends. Instead, doping appears to affect the methanation mechanism, and this is shown to play the most critical role in determining the catalytic performance. Both the RWGS+CO hydrogenation pathway and the formate pathway are identified as active CO_2 methanation mechanisms, with the former being dominant at lower temperature (below 250 °C). Cu addition inhibits those two pathways and results in a lower catalytic activity of Ni-Cu/SiO_2 compared with Ni/SiO_2. RWGS+CO hydrogenation pathway was promoted to the greatest extent by the Mn addition, and formate pathway could be enhanced to the greatest extent by the Co addition. Correspondingly, Ni-Mn/SiO_2 and Ni-Co/SiO_2 show the highest performance at lower (below 250 °C) and higher (above 300 °C) temperature, respectively.

Acknowledgements

YRZ thanks the CSC for his PhD fellowship. DPD thanks the Francqui Foundation for the Francqui Research Professor chair. François Devred is acknowledged for the technical and logistical help. The FCMat platform provides access to HRTEM facilities.

References

[1] N. Mac Dowell, P.S. Fennell, N. Shah, G.C. Maitland, The role of CO2 capture and utilization in mitigating climate change, Nature Climate Change, 7 (2017) 243–249.

[2] S.M. Kim, P.M. Abdala, M. Broda, D. Hosseini, C. Copéret, C. Müller, Integrated CO2 Capture and Conversion as an Efficient Process for Fuels from Greenhouse Gases, ACS Catalysis, 8 (2018) 2815–2823.

[3] R.E. Siegel, S. Pattanayak, L.A. Berben, Reactive Capture of CO2: Opportunities and Challenges, ACS Catalysis, 13 (2023) 766–784.

[4] L. Li, S. Miyazaki, S. Yasumura, K.W. Ting, T. Toyao, Z. Maeno, K.-i. Shimizu, Continuous CO2 Capture and Selective Hydrogenation to CO over Na-Promoted Pt Nanoparticles on Al2O3, ACS Catalysis, 12 (2022) 2639–2650.

[5] J.R. Khusnutdinova, J.A. Garg, D. Milstein, Combining Low-Pressure CO2 Capture and Hydrogenation To Form Methanol, ACS Catalysis, 5 (2015) 2416–2422.

[6] P. Hongmanorom, J. Ashok, P. Chirawatkul, S. Kawi, Interfacial synergistic catalysis over Ni nanoparticles encapsulated in mesoporous ceria for CO2 methanation, Applied Catalysis B: Environmental, 297 (2021) 120454.

[7] K. Mori, T. Taga, H. Yamashita, Isolated Single-Atomic Ru Catalyst Bound on a Layered Double Hydroxide for Hydrogenation of CO2 to Formic Acid, ACS Catalysis, 7 (2017) 3147–3151.

[8] L. Wang, S. He, L. Wang, Y. Lei, X. Meng, F.-S. Xiao, Cobalt–Nickel Catalysts for Selective Hydrogenation of Carbon Dioxide into Ethanol, ACS Catalysis, 9 (2019) 11335–11340.

[9] M.M.F. Hasan, L.M. Rossi, D.P. Debecker, K.C. Leonard, Z. Li, B.C.E. Makhubela, C. Zhao, A. Kleij, Can CO2 and Renewable Carbon Be Primary Resources for Sustainable Fuels and Chemicals?, ACS Sustainable Chemistry & Engineering, 9 (2021) 12427–12430.

[10] N. Rui, X. Zhang, F. Zhang, Z. Liu, X. Cao, Z. Xie, R. Zou, S.D. Senanayake, Y. Yang, J.A. Rodriguez, C.-J. Liu, Highly active Ni/CeO2 catalyst for CO2 methanation: Preparation and characterization, Applied Catalysis B: Environmental, 282 (2021) 119581.

[11] J. Li, A. Slassi, X. Han, D. Cornil, M.-H. Ha-Thi, T. Pino, D.P. Debecker, C. Colbeau-Justin, J. Arbiol, J. Cornil, M.N. Ghazzal, Tuning the Electronic Bandgap of Graphdiyne by H-Substitution to Promote Interfacial Charge Carrier Separation for Enhanced Photocatalytic Hydrogen Production, Advanced Functional Materials, 31 (2021) 2100994.

[12] X. Xu, H.-C. Chen, L. Li, M. Humayun, X. Zhang, H. Sun, D.P. Debecker, W. Zhang, L. Dai, C. Wang, Leveraging Metal Nodes in Metal–Organic Frameworks for Advanced Anodic Hydrazine Oxidation Assisted Seawater Splitting, ACS Nano, 17 (2023) 10906–10917.

[13] D. Xu, Y. Wang, M. Ding, X. Hong, G. Liu, S.C.E. Tsang, Advances in higher alcohol synthesis from CO2 hydrogenation, Chem, 7 (2021) 849–881.

[14] P.H. Ho, G.S. de Luna, S. Angelucci, A. Canciani, W. Jones, D. Decarolis, F. Ospitali, E.R. Aguado, E. Rodríguez-Castellón, G. Fornasari, A. Vaccari, A.M. Beale, P. Benito, Understanding structure-activity relationships in highly active La promoted Ni catalysts for CO2 methanation, Applied Catalysis B: Environmental, 278 (2020) 119256.

[15] W.L. Vrijburg, E. Moioli, W. Chen, M. Zhang, B.J.P. Terlingen, B. Zijlstra, I.A.W. Filot, A. Züttel, E.A. Pidko, E.J.M. Hensen, Efficient Base-Metal NiMn/TiO2 Catalyst for CO2 Methanation, ACS Catalysis, 9 (2019) 7823–7839.

[16] A. Quindimil, U. De-La-Torre, B. Pereda-Ayo, J.A. González-Marcos, J.R. González-Velasco, Ni catalysts with La as promoter supported over Y- and BETA- zeolites for CO2 methanation, Applied Catalysis B: Environmental, 238 (2018) 393–403.

[17] G. Garbarino, C. Wang, T. Cavattoni, E. Finocchio, P. Riani, M. Flytzani-Stephanopoulos, G. Busca, A study of Ni/La-Al2O3 catalysts: A competitive system for CO2 methanation, Applied Catalysis B: Environmental, 248 (2019) 286–297.

[18] X. Xu, L. Liu, Y. Tong, X. Fang, J. Xu, D.-e. Jiang, X. Wang, Facile Cr3+-Doping Strategy Dramatically Promoting Ru/CeO2 for Low-Temperature CO2 Methanation: Unraveling the Roles of Surface Oxygen Vacancies and Hydroxyl Groups, ACS Catalysis, 11 (2021) 5762–5775.

[19] Y. Wu, J. Lin, Y. Xu, G. Ma, J. Wang, M. Ding, Transition Metals Modified Ni−M (M=Fe, Co, Cr and Mn) Catalysts Supported on Al2O3−ZrO2 for Low-Temperature CO2 Methanation, ChemCatChem, 12 (2020) 3553–3559.

[20] L. Xu, Y. Cui, M. Chen, X. Wen, C. Lv, X. Wu, C.-e. Wu, Z. Miao, X. Hu, Screening Transition Metals (Mn, Fe, Co, and Cu) Promoted Ni-Based CO2 Methanation Bimetal Catalysts with Advanced Low-Temperature Activities, Industrial & Engineering Chemistry Research, 60 (2021) 8056–8072.

[21] Y. Zhao, V. Girelli, O. Ersen, D.P. Debecker, CO2 methanation with high-loading mesoporous Ni/SiO2 catalysts: Toward high specific activity and new mechanistic insights, Journal of Catalysis, 426 (2023) 283–293.

[22] M. Jacquemin, M.J. Genet, E.M. Gaigneaux, D.P. Debecker, Calibration of the X-Ray Photoelectron Spectroscopy Binding Energy Scale for the Characterization of Heterogeneous Catalysts: Is Everything Really under Control?, ChemPhysChem, 14 (2013) 3618–3626.

[23] A. Quindimil, U. De-La-Torre, B. Pereda-Ayo, A. Davó-Quiñonero, E. Bailón-García, D. Lozano-Castelló, J.A. González-Marcos, A. Bueno-López, J.R. González-Velasco, Effect of metal loading on the CO2 methanation: A comparison between alumina supported Ni and Ru catalysts, Catalysis Today, 356 (2020) 419–432.

[24] X. Guo, A. Traitangwong, M. Hu, C. Zuo, V. Meeyoo, Z. Peng, C. Li, Carbon Dioxide Methanation over Nickel-Based Catalysts Supported on Various Mesoporous Material, Energy & Fuels, 32 (2018) 3681–3689.

[25] P. Hongmanorom, J. Ashok, G. Zhang, Z. Bian, M.H. Wai, Y. Zeng, S. Xi, A. Borgna, S. Kawi, Enhanced performance and selectivity of CO2 methanation over phyllosilicate structure derived Ni-Mg/SBA-15 catalysts, Applied Catalysis B: Environmental, 282 (2021) 119564.

[26] Y. Yan, Y. Dai, Y. Yang, A.A. Lapkin, Improved stability of Y2O3 supported Ni catalysts for CO2 methanation by precursor-determined metal-support interaction, Applied Catalysis B: Environmental, 237 (2018) 504–512.

[27] S. Ding, L. He, L. Fang, Y. Zhu, T. Li, Z. Lyu, D. Du, Y. Lin, J.-C. Li, Carbon-Nanotube-Bridging Strategy for Integrating Single Fe Atoms and NiCo Nanoparticles in a Bifunctional Oxygen Electrocatalyst toward High-Efficiency and Long-Life Rechargeable Zinc–Air Batteries, Advanced Energy Materials, 12 (2022) 2202984.

[28] H. Chen, Y. Xia, R. Fang, H. Huang, Y. Gan, C. Liang, J. Zhang, W. Zhang, X. Liu, Effects of Nd-modification on the activity and SO2 resistance of MnOx/TiO2 catalysts for low-temperature NH3-SCR, New Journal of Chemistry, 42 (2018) 12845–12852.

[29] X. Peng, J. Zhang, T. Cen, Z. Ye, Y. Liu, D. Yuan, Co(OH)2-NiCo2O4 hybrid nanosheets coupled with N-doping reduced graphene oxide as efficient electrocatalysts for Zn-air batteries, Journal of Alloys and Compounds, 872 (2021) 159441.

[30] M. Sun, W. Zhang, Z. Liu, G. Wang, Direct observations on the crystal structure evolution of nano Cu-precipitates in an extremely low carbon steel, Materials Letters, 187 (2017) 49–52.

[31] K. Li, X. Chang, C. Pei, X. Li, S. Chen, X. Zhang, S. Assabumrungrat, Z.-J. Zhao, L. Zeng, J. Gong, Ordered mesoporous Ni/La2O3 catalysts with interfacial synergism towards CO2 activation in dry reforming of methane, Applied Catalysis B: Environmental, 259 (2019) 118092.

[32] B. Zhao, P. Liu, S. Li, H. Shi, X. Jia, Q. Wang, F. Yang, Z. Song, C. Guo, J. Hu, Z. Chen, X. Yan, X. Ma, Bimetallic Ni-Co nanoparticles on SiO2 as robust catalyst for CO methanation: Effect of homogeneity of Ni-Co alloy, Applied Catalysis B: Environmental, 278 (2020) 119307.

[33] P. Shafiee, S.M. Alavi, M. Rezaei, Solid-state synthesis method for the preparation of cobalt doped Ni–Al2O3 mesoporous catalysts for CO2 methanation, International Journal of Hydrogen Energy, 46 (2021) 3933–3944.

[34] Q. Liu, B. Bian, J. Fan, J. Yang, Cobalt doped Ni based ordered mesoporous catalysts for CO2 methanation with enhanced catalytic performance, International Journal of Hydrogen Energy, 43 (2018) 4893–4901.

[35] N. Gutta, V.K. Velisoju, A. Chatla, V. Boosa, J. Tardio, J. Patel, V. Akula, Promotional Effect of Cu and Influence of Surface Ni–Cu Alloy for Enhanced H2 Yields from CH4 Decomposition over Cu-Modified Ni Supported on MCM-41 Catalyst, Energy & Fuels, 32 (2018) 4008–4015.

[36] Z. Hao, J. Shen, S. Lin, X. Han, X. Chang, J. Liu, M. Li, X. Ma, Decoupling the effect of Ni particle size and surface oxygen deficiencies in CO2 methanation over ceria supported Ni, Applied Catalysis B: Environmental, 286 (2021) 119922.

[37] Y. Xie, J. Chen, X. Wu, J. Wen, R. Zhao, Z. Li, G. Tian, Q. Zhang, P. Ning, J. Hao, Frustrated Lewis Pairs Boosting Low-Temperature CO2 Methanation Performance over Ni/CeO2 Nanocatalysts, ACS Catalysis, 12 (2022) 10587–10602.

[38] H. Li, G. Lu, Q. Dai, Y. Wang, Y. Guo, Y. Guo, Efficient low-temperature catalytic combustion of trichloroethylene over flower-like mesoporous Mn-doped CeO2 microspheres, Applied Catalysis B: Environmental, 102 (2011) 475–483.

[39] Y. Yang, J. Huang, S. Wang, S. Deng, B. Wang, G. Yu, Catalytic removal of gaseous unintentional POPs on manganese oxide octahedral molecular sieves, Applied Catalysis B: Environmental, 142-143 (2013) 568–578.

[40] A.H. Braga, D.C. de Oliveira, A.R. Taschin, J.B.O. Santos, J.M.R. Gallo, J.M. C. Bueno, Steam Reforming of Ethanol Using Ni–Co Catalysts Supported on MgAl2O4: Structural Study and Catalytic Properties at Different Temperatures, ACS Catalysis, 11 (2021) 2047–2061.

[41] L.-C. Chen, S.D. Lin, The ethanol steam reforming over Cu-Ni/SiO2 catalysts: Effect of Cu/Ni ratio, Applied Catalysis B: Environmental, 106 (2011) 639–649.

[42] L. Roldán, Y. Marco, E. García-Bordejé, Origin of the Excellent Performance of Ru on Nitrogen-Doped Carbon Nanofibers for CO2 Hydrogenation to CH4, ChemSusChem, 10 (2017) 1139–1144.

[43] G. Varvoutis, M. Lykaki, E. Papista, S.A.C. Carabineiro, A.C. Psarras, G.E. Marnellos, M. Konsolakis, Effect of alkali (Cs) doping on the surface chemistry and CO2 hydrogenation performance of CuO/CeO2 catalysts, Journal of CO2 Utilization, 44 (2021) 101408.

[44] H. Muroyama, Y. Tsuda, T. Asakoshi, H. Masitah, T. Okanishi, T. Matsui, K. Eguchi, Carbon dioxide methanation over Ni catalysts supported on various metal oxides, Journal of Catalysis, 343 (2016) 178–184.

[45] Q. Pan, J. Peng, T. Sun, S. Wang, S. Wang, Insight into the reaction route of CO2 methanation: Promotion effect of medium basic sites, Catalysis Communications, 45 (2014) 74–78.

[46] L. Shen, J. Xu, M. Zhu, Y.-F. Han, Essential Role of the Support for Nickel-Based CO2 Methanation Catalysts, ACS Catalysis, 10 (2020) 14581–14591.

[47] J.F.M. Simons, T.J. de Heer, R.C.J. van de Poll, V. Muravev, N. Kosinov, E.J.M. Hensen, Structure Sensitivity of CO2 Hydrogenation on Ni Revisited, Journal of the American Chemical Society, 145 (2023) 20289–20301.

[48] C. Vogt, E. Groeneveld, G. Kamsma, M. Nachtegaal, L. Lu, C.J. Kiely, P.H. Berben, F. Meirer, B.M. Weckhuysen, Unravelling structure sensitivity in CO2 hydrogenation over nickel, Nature Catalysis, 1 (2018) 127–134.

[49] X. Xu, Y. Tong, J. Huang, J. Zhu, X. Fang, J. Xu, X. Wang, Insights into CO2 methanation mechanism on cubic ZrO2 supported Ni catalyst via a combination of experiments and DFT calculations, Fuel, 283 (2021) 118867.

[50] C. Cerdá-Moreno, A. Chica, S. Keller, C. Rautenberg, U. Bentrup, Ni-sepiolite and Ni-todorokite as efficient CO2 methanation catalysts: Mechanistic insight by operando DRIFTS, Applied Catalysis B: Environmental, 264 (2020) 118546.

[51] R.-P. Ye, Q. Li, W. Gong, T. Wang, J.J. Razink, L. Lin, Y.-Y. Qin, Z. Zhou, H. Adidharma, J. Tang, A.G. Russell, M. Fan, Y.-G. Yao, High-performance of nanostructured Ni/CeO2 catalyst on CO2 methanation, Applied Catalysis B: Environmental, 268 (2020) 118474.

[52] S. Zhang, S. Sun, B. Huang, N. Wang, X. Li, UV-Enhanced Formaldehyde Sensor Using Hollow In2O3@TiO2 Double-Layer Nanospheres at Room Temperature, ACS Applied Materials & Interfaces, 15 (2023) 4329–4342.

[53] C. Vogt, M. Monai, E.B. Sterk, J. Palle, A.E.M. Melcherts, B. Zijlstra, E. Groeneveld, P.H. Berben, J.M. Boereboom, E.J.M. Hensen, F. Meirer, I.A.W. Filot, B.M. Weckhuysen, Understanding carbon dioxide activation and carbon–carbon coupling over nickel, Nature Communications, 10 (2019) 5330.

Deciphering the role of dopants (Mn, Co, and Cu) in Ni-based CO_2 methanation catalysts

Electronic Supporting Information

Yingrui Zhao,[a] Sandra Casale, [b] Capucine Sassoye,[c] Damien P. Debecker [a,*]

[a] Université catholique de Louvain (UCLouvain), Institute of Condensed Matter and Nanosciences (IMCN), Place Louis Pasteur, 1, box L4.01.09, 1348 Louvain-La-Neuve, Belgium.
[b] Sorbonne Université, Laboratoire de Réactivité de Surface, CNRS UMR 7197, 4 Place Jussieu, 75005, Paris, France
[c] Sorbonne Université, Chimie de la Matière Condensée de Paris, UMR 7574, 4 Place Jussieu, 75005 Paris, France.

* Corresponding autor:
E-mail: damien.debecker@uclouvain.be
ORCID: 0000-0001-6500-2996

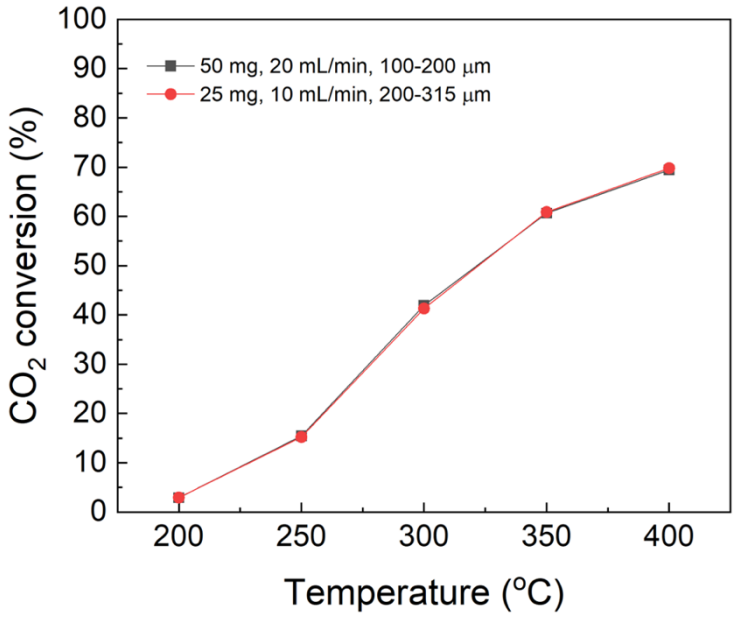

Fig. S1. CO_2 conversion over the Ni/SiO_2 at different condition.

To decrease the contacting time and keep the GHSV at 24000 mL g^{-1} h^{-1}, the weight of sample and the total flow rate (CO_2:H_2:He is still 1:4:5) decreased to 25 mg and 10 mL/min, separately. The catalyst pellets increase to 200-315 μm and diluted by SiO_2. We can find that there is no obvious change of the CO_2 conversion at each testing temperature, confirming no mass and heat transfer limitation existing in the tested condition.

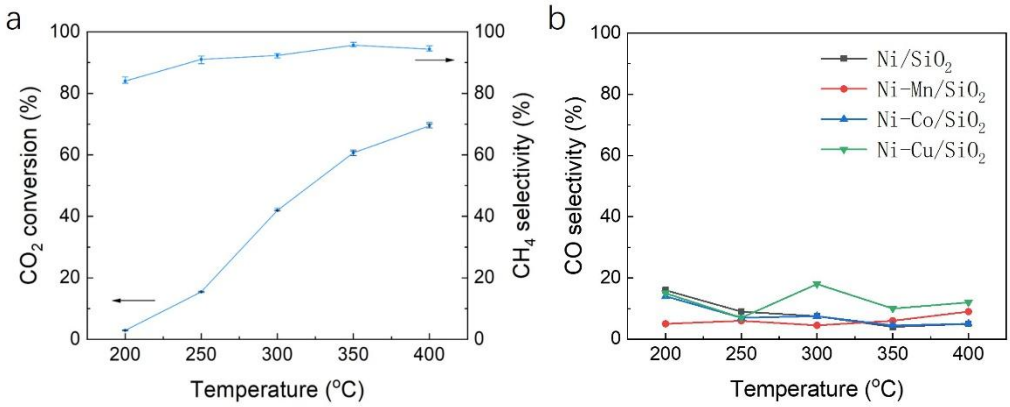

Fig. S2. (a) CO_2 conversion and CH_4 selectivity obtained over a test in triplicate with Ni/SiO_2 (error bars show the standard deviation). Reaction conditions: 10% CO_2, 40% H_2, balance He; total flow rate 20 mL min^{-1} (GHSV = 24,000 mL g^{-1} h^{-1}). (b) CO selectivity as a function of temperature. Reaction conditions: 10% CO_2, 40% H_2, balance He; total flow rate 20 mL min^{-1} (GHSV = 24,000 mL g^{-1} h^{-1}).

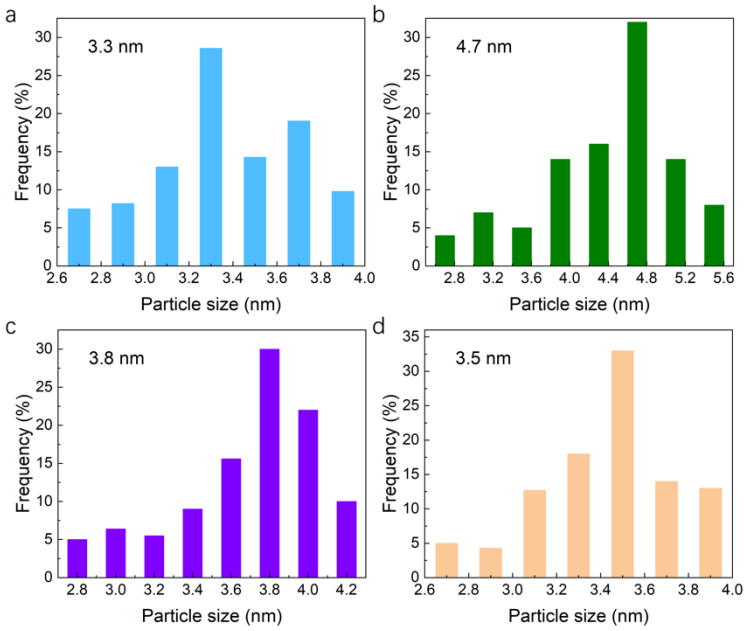

Fig. S3. Ni particles size distribution of (a) Ni/SiO_2, (b) $Ni\text{-}Mn/SiO_2$, (c) $Ni\text{-}Co/SiO_2$, (d) $Ni\text{-}Cu/SiO_2$.

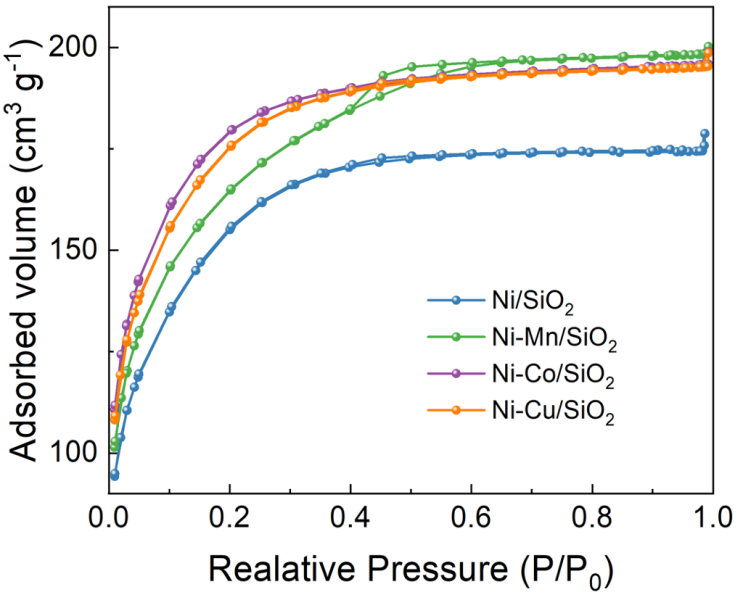

Fig. S4. N_2 adsorption-desorption isotherms.

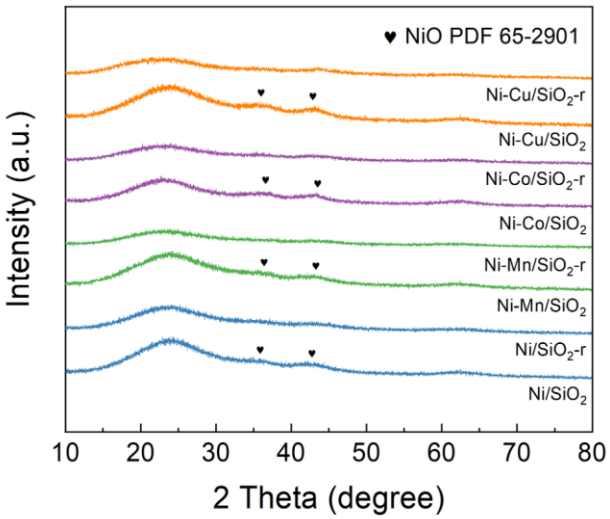

Fig. S5. XRD patterns of the calcined and reduced catalysts.

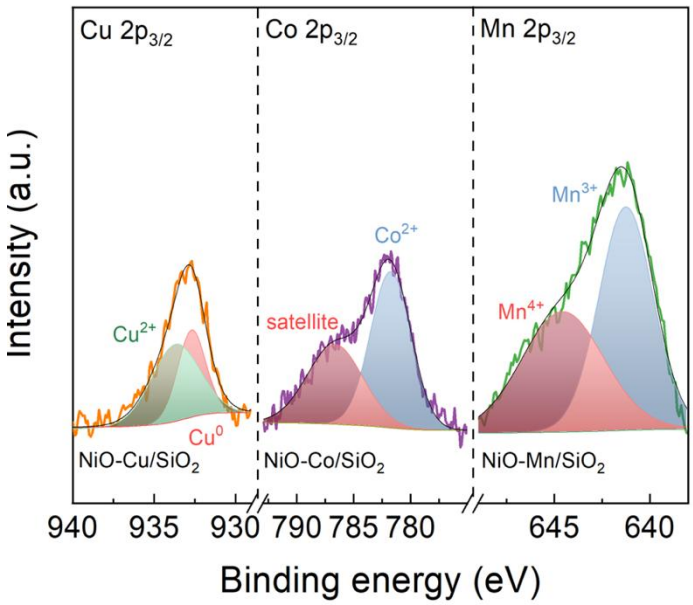

Fig. S6. XPS spectra of Mn $2p_{3/2}$, Co $2p_{3/2}$, and Cu $2p_{3/2}$ over the calcined catalysts.

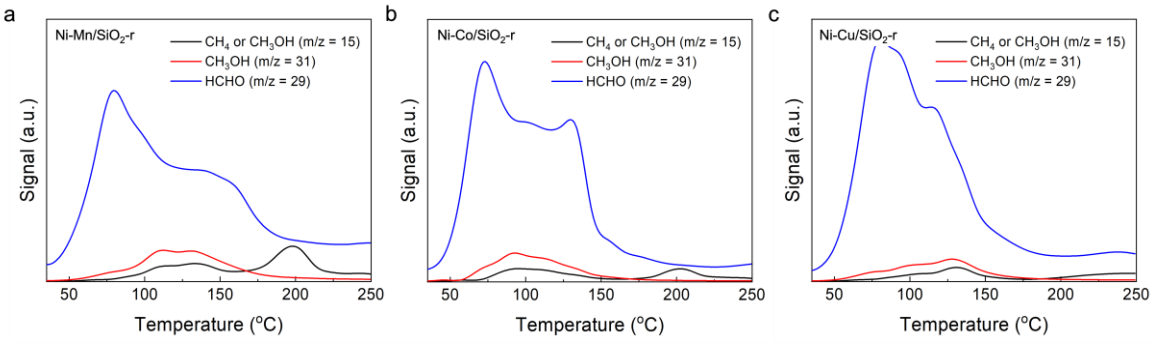

Fig. S7. HCHO-TPSR over reduced Ni-M/SiO_2.

Table S1. CO_2 conversion and CH_4 selectivity of prepared catalyst tested at high GHSV = 172,800 mL g^{-1} h^{-1}

Catalyst	T (°C)	CO_2 conversion (%)	CH_4 selectivity (%)
Ni-Mn/SiO_2-r	250	3.5	93
Ni-Co/SiO_2-r		2.4	92
Ni/SiO_2-r		6.5	92
Ni-Mn/SiO_2-r	300	9.9	95
Ni-Co/SiO_2-r		14.8	92
Ni-Cu/SiO_2-r		3.3	82

To calculate the TOF, we increased the GHSV to keep the CO_2 conversion below 15%.